

How Does Subsurface Characterization Affect Simulations of Hyporheic Exchange?

by Adam S. Ward^{1,2}, Michael N. Gooseff³, and Kamini Singha⁴

Abstract

We investigated the role of increasingly well-constrained geologic structures in the subsurface (i.e., subsurface architecture) in predicting streambed flux and hyporheic residence time distribution (RTD) for a headwater stream. Five subsurface realizations with increasingly resolved lithological boundaries were simulated in which model geometries were based on increasing information about flow and transport using soil and geologic maps, surface observations, probing to depth to refusal, seismic refraction, electrical resistivity (ER) imaging of subsurface architecture, and time-lapse ER imaging during a solute tracer study. Particle tracking was used to generate RTDs for each model run. We demonstrate how improved characterization of complex lithological boundaries and calibration of porosity and hydraulic conductivity affect model prediction of hyporheic flow and transport. Models using hydraulic conductivity calibrated using transient ER data yield estimates of streambed flux that are three orders of magnitude larger than uncalibrated models using estimated values for hydraulic conductivity based on values published for nearby hillslopes (10^{-4} vs. 10^{-7} m²/s, respectively). Median residence times for uncalibrated and calibrated models are 10^3 and 10^0 h, respectively. Increasingly well-resolved subsurface architectures yield wider hyporheic RTDs, indicative of more complex hyporheic flowpath networks and potentially important to biogeochemical cycling. The use of ER imaging to monitor solute tracers informs subsurface structure not apparent from other techniques, and helps to define transport properties of the subsurface (i.e., hydraulic conductivity). Results of this study demonstrate the value of geophysical measurements to more realistically simulate flow and transport along hyporheic flowpaths.

Introduction

The ecological relevance of exchange flows between streams and their hyporheic zones (i.e., near-stream aquifers) has been widely recognized in the past 20 years

(see reviews by Brunke and Gonser 1997; Boulton et al. 2010; Krause et al. 2010) yet our ability to model hyporheic exchange with high spatial resolution lags behind our understanding of the associated biogeochemical processes occurring along these flowpaths. Wondzell et al. (2009) summarize the growing interest in numerical groundwater flow modeling as a tool to improve our understanding of solute transport in coupled stream-hyporheic systems in four areas: (1) quantifying the location and magnitude of fluxes across the streambed; (2) quantifying residence time distributions (RTDs) of water along hyporheic flowpaths; (3) providing a spatially explicit depiction of flowpaths; and (4) examining the factors that control hyporheic exchange. Indeed, numerical models of hyporheic flow and transport have been widely used in studies of hyporheic exchange (e.g., Kasahara and Wondzell 2003; Saenger et al. 2005; Gooseff et al. 2006; Lautz and Siegel 2006; Wondzell et al. 2009).

¹Department of Civil and Environmental Engineering, The Pennsylvania State University, University Park, PA 16802.

²Corresponding author: Department of Geoscience, The University of Iowa, 36 Trowbridge Hall, Iowa City, IA 52242; 319-353-2079; fax: 319-335-1821; adam-ward@uiowa.edu

³Department of Civil and Environmental Engineering, The Pennsylvania State University, University Park, PA 16802; 814-867-0044; mgooseff@enr.psu.edu

⁴Department of Geosciences, The Pennsylvania State University, University Park, PA 16802; 814-863-6649; ksingha@psu.edu

Received August 2011, accepted January 2012.

© 2012, The Author(s)

Ground Water © 2012, National Ground Water Association.

doi: 10.1111/j.1745-6584.2012.00911.x

Despite the promise and utility of numerical modeling to inform our understanding of solute transport in coupled stream-hyporheic systems, accurate representation of real-world systems in such models is problematic, if not impossible, due to heterogeneity in the subsurface. Subsurface heterogeneity at the sub-unit scale is both difficult to characterize and serves as a primary control on stream-aquifer interactions (e.g., Packman and Salehin 2003; Ryan and Boufadel 2006; Sawyer and Cardenas 2009). Increasing heterogeneity at the sub-unit scale has been linked with increased exchange flux (Cardenas et al. 2004; Salehin et al. 2004). At larger scales, heterogeneity in subsurface architecture (i.e., heterogeneities occurring at a macroscopic scale, such as different geologic units, sediment types, etc.), as opposed to variability occurring within a given unit, may control exchange flux. For example, valley constraint of lateral and vertical flowpaths or bedrock confining units can limit the extent of hyporheic flowpaths (Vaux 1968; Ward et al. 2011).

The challenge of characterizing heterogeneity in the subsurface is central to the equifinality thesis (i.e., non-uniqueness of model parameterization) as applied to hyporheic exchange modeling (i.e., the thesis that multiple realizations of the subsurface may produce equally good fits based on data observed at discrete locations; e.g., Beven 2006). Indeed, a long-standing debate exists in the literature regarding whether such models can ever be verified or validated given the documented equifinality (e.g., Konikow and Bredehoeft 1992; Bredehoeft and Konikow 1993; Oreskes et al. 1994; Hassan 2004). Most recently, Wondzell et al. (2009) extended these issues to include models of stream-aquifer interactions, finding equally acceptable performance from homogeneous subsurface models with idealized boundaries and models including heterogeneity and more complex boundary topography. Their study finds simplified models acceptable to predict fluxes and approximate travel times at the stream reach scale, but they conclude that such simple models are not sufficient to predict the movement of solutes through the hyporheic zone with high levels of confidence, which is a desired outcome for simulating pollutant fate and transport along these flowpaths.

In contrast to direct probing or sampling of the subsurface, which directly disturbs the system being studied, geophysical methods can be used to characterize subsurface structure, hydrological parameters, and monitor transport processes (Binley et al. 2010). Hydrogeophysical characterization of the subsurface can be described as either of two types of features: process areas, or geologic properties that do not change over time, and process dynamics, or characteristics that change through time and are inherently linked to the movement of fluids (primarily water) in the subsurface (Koch et al. 2009; Binley et al. 2010). Indeed, geophysical investigation to characterize process areas for study of hyporheic exchange is growing in popularity, with demonstrated application of electrical resistivity (ER) (e.g., Crook et al. 2008; Ward et al. 2010b), ground-penetrating radar (e.g., Naegeli et al. 1996; Jones et al. 2008; Brosten et al. 2009), and seismic

refraction and reflection (e.g., Anderson et al. 2005; Jones et al. 2008). These techniques can be used to characterize subsurface architecture based on changes in the geophysical properties of the subsurface and commonly produce continuous spatial distributions of such properties (e.g., ER, compressional wave velocity). Geologic structure is inferred from the spatial distribution of geophysical properties. Linking geophysical properties with hydrologic properties (e.g., correlation of ER and hydraulic conductivity) requires development of site-specific relationships, which has had limited success because of high levels of uncertainty (e.g., Day-Lewis et al. 2005; Lesmes and Friedman 2005; Pride 2005; Singha and Moysey 2006). Although direct inference of hydrological properties from geophysical properties is limited in its application, the strength of geophysical investigation has long been the ability to characterize subsurface structure, which is then informed through other measurements (e.g., boreholes).

Although the use of geophysics to study process areas (i.e., static features in the subsurface) has been an active area of research, the application of geophysical methods to study process dynamics in hyporheic zones has been limited to date. Nyquist et al. (2008) used ER to characterize locations of groundwater discharge to a stream. Binley et al. (2010) suggest that perturbing a system using a controlled experiment over relatively short time scales (hours to weeks) and rapid collection of geophysical data might be the most informative application of geophysics to characterize subsurface hydrologic properties. Although not hyporheic in application, several studies suggest ER imaging of solute tracers could be an informative technique to characterize hydrologic process dynamics. One such example is work by Slater et al. (1997), who identified preferential flow through fractures using saline tracers and electrical geophysical monitoring. ER imaging of saline tracers has been used to inform groundwater flow properties (e.g., White 1988; Bevc and Morrison 1991) including preferential flowpaths (e.g., Schima et al. 1996), and have been used to parameterize numerical models of flow and transport in the subsurface (Binley et al. 1996b; Kemna et al. 2002). Indeed, saline tracers have recently been used to characterize hyporheic exchange in both field (Nyquist et al. 2008; Ward et al. 2010b) and numerical studies (Singha et al. 2008; Ward et al. 2010a).

The objective of this study is to determine how increasingly well-constrained realizations of complex subsurface architecture affect model simulations of hyporheic RTDs and total flux across the streambed (i.e., hyporheic exchange flux). In this study, we used field observations of both static features and dynamic solute transport to characterize hydraulic conductivity distributions in the subsurface and then calibrate groundwater flow models of hyporheic exchange in a first-order stream overlying a shale bedrock site using transient ER data. We created five uncalibrated models, parameterized by cumulatively considering different amounts of data: (1) surface observations at the site, soils maps, and geologic maps of the site; (2) depth-to-refusal measurements to parameterize topography between weathered shale and

overlying sediment; (3) seismic refraction to characterize the boundary between underlying weathered and unweathered bedrock; (4) static ER imaging to more completely constrain subsurface architecture; and (5) transient ER data. Each subsequent model used the previous as a starting point, and added refinement of lithological boundaries based on the new data collected. For the most constrained numerical model above (i.e., using data from all investigation methods, (5) above), we used coupled solute transport and time-lapse ER imaging to calibrate hydraulic conductivity for the subsurface lithology simulated. Through both qualitative (i.e., pseudo-3D visualization) and quantitative (i.e., temporal moment analysis) interpretation of a coupled solute tracer and ER experiment, our numerical model was calibrated to match observations of subsurface solute transport collected using ER imaging. Results of this study inform the role of subsurface architecture in hyporheic exchange and illustrate limitations of poorly constrained models in predicting the spatial extent of hyporheic flowpath networks, their RTDs, and hyporheic exchange flux.

Methods

Site Description

Watershed #1 at the Leading Ridge Watershed Research Unit (near State College, Pennsylvania) is a small, forested watershed draining 0.43 km². Typical valley slopes are 4 to 5%, with a southeastern aspect. The site is covered with even-age forests including oak, hickory, and maple trees, uncut since commercial logging in the 1840s and 1900s (Kostelnik et al. 1989). Watershed #1 is a control watershed, with limited harvesting since the research unit was established in the 1960s (Rishel et al. 1982). Topography at the research site is relatively flat. The stream draining Watershed #1 is 1.5 to 2 m wide and 0.1 to 0.2 m deep through the study reach, with a gradient of approximately 2% along the centerline in the surveyed reach. The stream and watershed react quickly to storm events, with response lagging precipitation by only about 30 min (Lynch and Corbett 1989). Runoff response in the watershed is primarily a subsurface flow to the stream, as opposed to overland flow (Lynch and Corbett 1989). The research site and instrumentation are shown in Figure 1.

Soils at the surface are generally high in organic matter, typical of a hardwood forest floor, and are primarily residual, having developed as a result of in situ weathering of the underlying strata. The research site is underlain by three primary soil types: Brinkerton silt loam, Edom-Weikert complex, and Newark silt loam. All three soil series are primarily silt and stony loams that are well drained. Soils are 8 to 200+ cm deep and range from 21.0 to 42.8% clay in content (USDA-NRCS 2008). A shallow seismic study by Shields and Sopper (1969) on the upper slopes of the watershed identified weathered shale layers averaging 3.2 m thick, lying below 1.4 m of soil.

The site is located in the Appalachian Mountain Section of Pennsylvania's Ridge and Valley Province

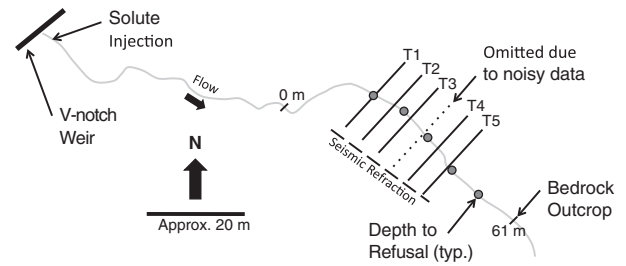


Figure 1. Geophysical studies and a constant-rate solute injection (20.8-h drip of NaCl into the stream) were performed at the Leading Ridge Experimental Watershed near State College, Pennsylvania. Depth to refusal was recorded by driving a 2.54 cm diameter steel rod into the streambed at five locations, and a bedrock outcrop was observed in the stream at the downstream end of the study reach. ER data were collected along six two-dimensional transects of 12 electrodes each (2 m electrode spacing) perpendicular to the stream, with transects spaced approximately 4 m along the stream centerline. Data from one transect were omitted from the study because they were too noisy to produce ER images of the subsurface. Seismic refraction data were collected along a single transect parallel to the stream. Flow at the V-notch weir was 0.6 L/s during the study.

(Sevan 2000). Most of the lower slope is underlain by the Rose Hill shale formation (~200-m thick). The upper portion of the lower and middle slopes are underlain by the Castanea sandstone (~150-m thick), and the ridge top is underlain by the Tuscarora quartzite (Lynch et al. 1986). Within the Rose Hill shale formation, layers of sandstone and siltstone were observed at an outcrop along the stream centerline at the downstream end of the study reach.

Subsurface Characterization for Development of Lithology-Based Models

Direct Investigation of the Subsurface

Direct observation of the thickness of alluvium and location of subsurface features was completed by driving a 2.54-cm diameter steel rod into the streambed at the stream centerline until refusal. This refusal was interpreted as the interface between the weathered shale layer and overlying streambed sediment matrix. We assume an unweathered bedrock layer exists at some depth below the weathered shale, based on previous studies at the site (Shields and Sopper 1969) and because an outcrop of this bedrock is observed at the downstream end of the study reach. Observation locations and refusal depths are shown in Figure 2. Stream topography and locations of measurements were surveyed using a sight level and tape.

Seismic Refraction Survey

Shallow seismic refraction data were collected along the transect labeled "seismic refraction" in Figure 1. Data were recorded on a seismograph manufactured by Geometrics Inc. (San Jose, California), using 24 geophones at 1 m spacing. The seismic transect was located approximately perpendicular to the ER transects and parallel to the stream (offset from the stream by

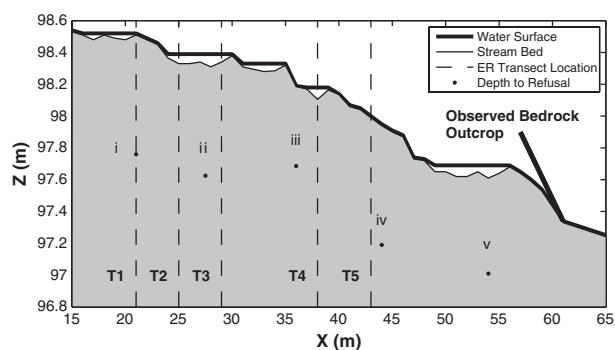


Figure 2. Longitudinal profile of the study reach geomorphology based on topographic survey. The longitudinal location of ER transects (dashed lines) and depth-to-refusal measurements (black dots) are shown. The water surface shown was calculated using the surface hydraulics model HEC-RAS (Brunner 2006) with observed topography and flow rate (at the upstream weir). A bedrock outcrop was observed beginning at $X = 61$ m and continuing downstream beyond the extent of the study reach.

approximately 10 m). Shot offset was 1 m from the geophone array for both the forward and reverse shots, respectively located at the southeast and northwest ends of the transect. Data were collected across a relatively flat topography, with total elevation changes of 0.57 m along the transect. No terrain correction (time delay) was assigned based on topography.

Visual interpretation of seismograms was used to identify first arrival times at each geophone. For consistency, a single interpreter identified all first arrival times based on graphical output from the seismograph. Assuming that all first arrivals identified were prone to a random (rather than systematic) error, the procedure of using best-fit lines for the data minimizes the error associated with any individual observation.

The data were interpreted as a three-layer system (soil, weathered shale, and unweathered bedrock) with plane-bed interfaces, based on available soil and geologic data. The upper interface (between our interpreted soil and weathered shale layers) could also represent the location of the water table. As no borehole logs were completed to confirm this, only the shale-bedrock interface (below the water table) was used to parameterize the flow and transport models. Average slopes for the forward and reverse shots were used to calculate velocities for each layer. The slope-intercept method was used to estimate thicknesses for the top two layers. The program REFRACT (Burger et al. 2006) was used to develop a subsurface model that best fit the observed seismic data (as minimum root-mean square error, RMSE, between observed and simulated data). The initial model was based on thicknesses estimated from the forward shot, and layer velocities estimated from the slope and intercept of arrival data. The subsurface architecture of the layers (i.e., layer thicknesses, dip angles) was determined by manually adjusting REFRACT model parameters to achieve a best fit, and was completed independently of other subsurface characterization data.

ER Imaging

ER data were collected in a series of six transects oriented perpendicular to the stream channel at distances of 70 to 92 m downstream of the injection location (hereafter T1 through T5, Figure 1; located at X -coordinates 21 through 43 m, Figure 2), using an Syscal Pro Switch (IRIS Instruments, Orleans, France). No ER data were collected parallel to the stream channel (e.g., as a transect along the stream centerline) in an effort to maximize temporal resolution of the data set collected. ER data for each transect were collected using 12 electrodes at a 2-m spacing approximately centered on the stream. ER data were collected only along transects (e.g., no measurements were collected using electrodes between multiple transects). One hundred sixty-six unique quadripoles (measurements consisting of a potential pair and current pair of electrodes) were collected using a modified dipole-dipole scheme. Two replicate measurements were collected for each quadripole and stacked (i.e., averaged); a third measurement was collected and included in the stacking if there was a greater than 3% difference between the first two measurements. Errors were not quantified using reciprocal measurements to maximize temporal resolution within the data set.

After collection of one complete data set, a constant-rate injection (~ 1 mL/s) of dissolved sodium chloride (NaCl, 61.9 mS/cm) into the stream channel immediately downstream of the V-notch weir was conducted for 20.8 h. In-stream flow during the study was 0.6 L/s, determined at the V-notch weir. Additional details on the tracer study are presented in Ward et al. (2010b). Data were collected at each transect approximately every 1.5 h, and stationarity was assumed during the collection time for each transect (i.e., it was assumed solute tracer distribution did not change during the 15-min collection time for each transect).

ER data were inverted using EarthImager2D (Advanced Geosciences Inc. 2008), which seeks the smoothest possible subsurface model of ER to explain the subsurface architecture. Horizontal and vertical block sizes ranged from 0.5 to 1.0 m and 0.07 to 0.18 m, respectively. A uniform starting model was used to invert background (i.e., pre-tracer) data. Time-lapse inversion was used to develop subsurface models for ER data collected during the injection, with the previous timestep used as the starting model for subsequent inversions. The background ER model was used as the starting model for the first timestep. The background (i.e., pre-tracer injection) model was subtracted from the time-lapse models, and the percent change from background was calculated for each pixel. The presence of the electrically conductive tracer is recorded when a drop in ER (i.e., negative percent change) was predicted in the inverted images. It is important to note that ER imaging is non-exact, and that inversion results (i.e., subsurface models) are non-unique. Results are sensitive to the inversion scheme, regularization of the model, and parameterization of the inversion process (e.g., Friedel 2003; Day-Lewis et al. 2005) and result in over-smoothed representations

of the subsurface due to diffusive physics governing electrical fields and the inversion scheme (Day-Lewis et al. 2005).

The resulting 2D inversion models were located in three-dimensional (3D) space based on field-surveyed locations, and linear interpolation between these 2D “slices” was used to construct pseudo-3D images of the hyporheic zone. We chose not to invert the data in 3D because of the limited data collection scheme (collection only along, and not between, transects), and to minimize the parameters necessary for data inversion. We acknowledge that linear interpolation over distances of 4 to 8 m between transects may not produce data that are representative of heterogeneities at all scales, but we believe that there is value in identifying trends between transects where ER data and models are available. This interpolation provides a tool to identify the subsurface architecture at a macroscale (i.e., features on the order of meters). A 3.5% change from background was selected as a threshold to parse changes due to solute presence from those due to both noise in the data collection and error in the inversion process (after Ward et al. 2010b). This threshold was selected for this specific data set and should be evaluated for other applications.

Numerical Modeling

Model Formulation

The finite-element model COMSOL (COMSOL 2008) was applied in a 2D space along the stream thalweg to solve the steady-state groundwater flow equation. The bottom boundary of the model was treated as a no-flow boundary, fixed at the average slope of the stream topography within the reach. An average subsurface depth of 8 m was simulated; iterative simulations of varying depths showed no hyporheic flowpaths reached this depth, and model results for a given geometry were insensitive to changes in overall subsurface depth because of the thick, low hydraulic conductivity shale simulated in the deep subsurface. The computational mesh ranged from approximately 71,000 to 84,000 elements; average element quality ranged from 0.982 to 0.995. Average element size is approximately $1.6 \times 10^{-2} \text{ m}^2$. Stream flow over the surveyed streambed topography was simulated using the U.S. Army Corps of Engineers’ 1D surface flow model HEC-RAS (Brunner 2006) to calculate a steady-state water surface through the study reach. HEC-RAS flow depths were applied as a constant-head boundary along the upper extent of the groundwater flow model. No iteration between up- and downwelling predicted by COMSOL and HEC-RAS flow rates was completed, as past studies have found this step unnecessary for hydraulic conductivities less than 10^{-2} m/s (Hester and Doyle 2008). To condition the inflow to the study reach in the subsurface, we simulated an additional 21 m of stream length (parameterized by observed topography) upstream of the study reach in both the HEC-RAS and COMSOL models. Finally, in the COMSOL model, we extended the upstream and downstream slopes and constant heads

an additional 40 m in both directions to isolate the upstream and downstream boundaries of the COMSOL model (constant-head boundaries) from the study reach of interest. Subsurface architecture was extended upstream and downstream in layers parallel to the streambed for the domains outside of the study reach.

Flow and transport parameters for the bedrock, less-weathered shale, weathered shale, and overlying streambed sediment (from deepest to shallowest) were assumed homogeneous and isotropic; hydrogeologic parameters for each layer are summarized in Table 1. Five realizations of subsurface architecture (i.e., five model geometries), as informed by a variety of tools as discussed in preceding sections, were simulated to represent our interpretation of the subsurface based on increasing information about flow and transport (summarized in Table 2).

Total flux across the streambed was computed using trapezoidal integration of flux magnitudes within the study reach (i.e., $21 < X < 61 \text{ m}$, Figure 2). The integration combines both up- and downwelling fluxes into a single parameter representing gross exchanges of water across the streambed (after Ward et al. 2011). To characterize the residence times of hyporheic flowpaths, we used particle-tracking tools in COMSOL. Particle tracking has been used to quantify upwelling and downwelling locations (e.g., Gooseff et al. 2006) and hyporheic RTDs (Wroblicky et al. 1998; Ward et al. 2011). This technique is only able to quantify timescales of advective transport in the subsurface (Lautz and Siegel 2006), with effective porosities used to convert Darcian to advective velocities for particle tracking. Particles were released at 2.5-cm spacing along the streambed and were tracked until they exited the subsurface domain. Particle releases were not flux weighted, and particle-tracking timesteps were non-uniform and automatically tuned by COMSOL (after Ward et al. 2011). We did not test for mesh sensitivity with respect to particle tracking.

Model Calibration by Temporal Moment Analysis

Temporal trends in solute transport through the matrix can be characterized by the analysis of individual pixels (i.e., elements) in the inverted images (Binley et al. 1996a; Slater et al. 2000, 2002). Here, we calculate the k th normalized temporal moment for the change in resistivity in each pixel using the equation

$$n_k = \int_0^{+\infty} r(t)t^k dt \quad (1)$$

where t is time, and $r(t)$ is the normalized change in pixel resistivity, which is calculated as

$$r(t) = \frac{R(t)}{\int_{-\infty}^{+\infty} R(t)dt} \quad (2)$$

where $R(t)$ is the resistivity change of the pixel. The normalized first moment (n_1/n_0) is physically interpreted as the mean arrival time for the tracer at the pixel location. For this study, only normalized first temporal moments

Table 1
Hydrogeologic Properties of Simulated Geologic Units

Geologic Unit	Uncalibrated Values		Calibrated Values	
	Porosity (%)	Hydraulic Conductivity (m/s)	Porosity (%)	Hydraulic Conductivity (m/s)
Streambed sediment	14.00	1.0×10^{-7}	25.00	8.0×10^{-5}
Weathered shale	21.15	8.3×10^{-8}	25.00	8.0×10^{-5}
Unweathered shale	12.33	5.0×10^{-11}	12.33	5.0×10^{-11}
Bedrock	0.35	2.7×10^{-15}	0.35	2.7×10^{-15}

Notes: Values are within the ranges for the local soils and shale presented by Kuntz et al. (2011) for a nearby site and those for weathered shale values in Mayes et al. (2000). Calibrated values were based on matching observed mean arrival times (based on first temporal moments of time-lapse ER images) with simulated particle arrival times. Hydrogeologic values for unweathered shale and bedrock were not changed from values reported by Kuntz et al. (2011) and Mayes et al. (2000).

Table 2
Summary of Model Runs, Streambed Flux, and RTDs Summary for Alternative Models of Subsurface Architecture (runs 1 to 5) and for Calibrated vs. Uncalibrated Hydrogeologic Parameterization (run 5 vs. run 6)

Model Run No.	Geometry	Subsurface Characterization	Hydrogeologic Parameters	Total Streambed Flux ¹ (m ² /s)	Mean Residence Time (h)	Median Residence Time (h)	Variance of Residence Times (h ²)
1	A	Soil + geologic maps, surface observations	Uncalibrated ²	1.01×10^{-6}	9.5×10^4	5.4×10^3	5.0×10^{10}
2	B	A + depth to refusal	Uncalibrated ²	7.44×10^{-7}	9.3×10^6	4.6×10^3	1.3×10^{17}
3	C	B + seismic refraction	Uncalibrated ²	7.33×10^{-7}	1.2×10^8	2.3×10^3	8.0×10^{18}
4	D	C + background ER	Uncalibrated ²	7.04×10^{-7}	1.3×10^{10}	2.2×10^3	2.6×10^{23}
5	E	D + solute tracer ER	Uncalibrated ²	6.62×10^{-7}	5.9×10^6	3.5×10^3	1.2×10^{15}
6	E	D + solute tracer ER	Calibrated ³	3.53×10^{-4}	1.5×10^9	6.6 × 10	1.7×10^{21}

¹Flux is reported as m/s multiplied by a unit streambed width.
²Uncalibrated hydrogeologic parameters are based on published values for nearby sites (Table 1).
³Geometry E was used to calibrate hydrogeologic parameters for the soil and weathered shale layers. Calibration was based on a visual best-fit matching mean arrival time from time-lapse ER imaging with particle arrival times.

were calculated from the time-lapse images. Mean arrival time based on individual pixels in the ER data were compared to the simulated arrival time of particles at corresponding locations in the model to calibrate hydraulic conductivity for each model unit.

Simulations of flow and transport for all five geometries were run using uncalibrated values of porosity and hydraulic conductivity (based on values in the literature for studies published at nearby sites and using similar materials; Table 1). Using the most well-resolved starting model (Geometry E, which integrated all subsurface investigation techniques), simulated particle arrival times at T4 and T5 were compared to the mean arrival times in corresponding pixels observed in the ER data along the stream centerline at these locations. Data from T1 through T3 were omitted from this analysis because flowpaths intersecting these planes (and associated particle arrival times) at these locations are dependent upon subsurface architecture upstream of T1. As we did not characterize the subsurface upstream of T1 to the degree that we can condition the subsurface inflow to the upstream end of

our model, our confidence in the results at these transects, particularly for the purposes of model calibration, is limited. The hydrogeologic properties of the streambed sediment and weathered shale layers (i.e., hydraulic conductivity, porosity) were adjusted to calibrate each model based on the ER data; weathered shale and bedrock parameters did not need to be adjusted to match particle arrival times with temporal moments at the order-of-magnitude scale. Calibration was determined by producing the best agreement between observed mean arrival times (i.e., first temporal moments of individual pixels in time-lapse ER images) and simulated particle arrival times at each transect. Assumptions of homogeneity and isotropy within each unit were maintained for the calibration.

Summary of Numerical Modeling

Five uncalibrated realizations of the subsurface were created, based on varying amounts of subsurface data from field characterization. The lithological boundaries determined from these data were filled with hydrogeologic parameter values (i.e., hydraulic conductivity, porosity)

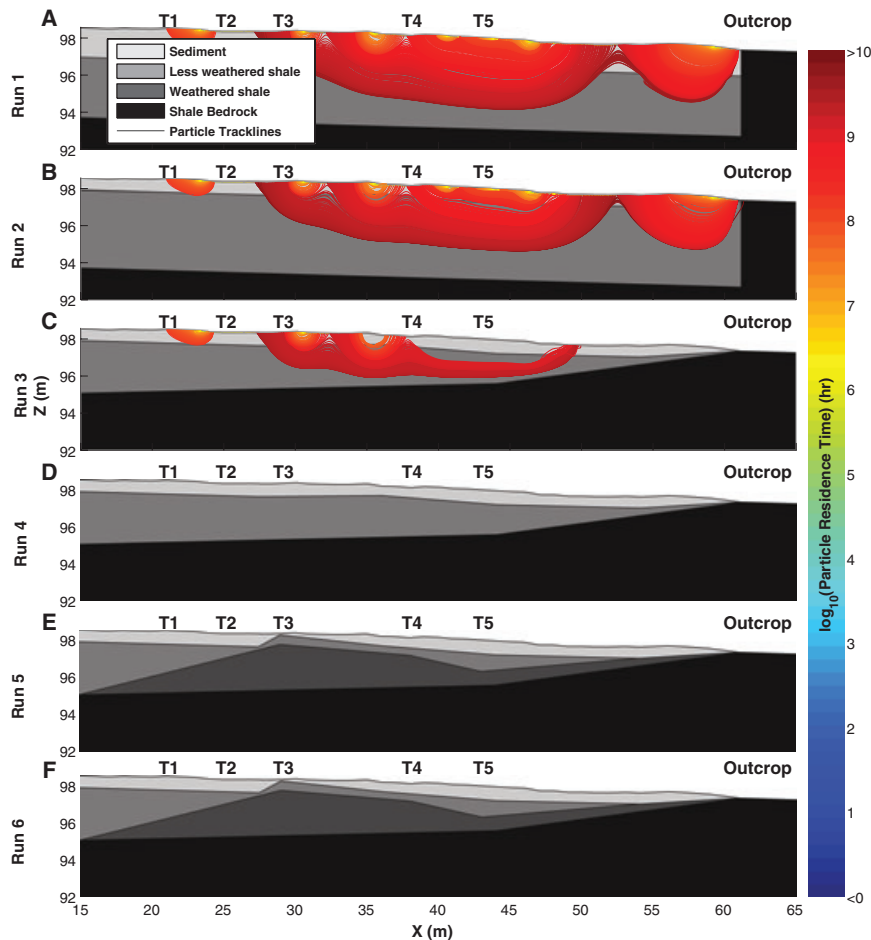


Figure 3. Five conceptual geometries for subsurface architecture, with lithological boundaries cumulatively informed by (A) soils and geologic maps and site observations, (B) depth-to-refusal measurements, (C) seismic refraction to identify topography of the bedrock interface, (D) ER imaging of background conditions, and (E) ER imaging during an electrically conductive solute tracer study. Up to four geologic units (sediment, weathered shale, less-weathered shale, and shale bedrock) were simulated (each homogeneous and isotropic; hydrogeologic parameters summarized in Tables 1 and 2). (F) Results for Geometry E using calibrated hydrogeologic parameters.

from published studies (model runs 1 to 5). Flux and RTDs were then calculated for each “uncalibrated” model run. Next, the most-constrained model geometry (Geometry E) was used to calibrate hydrogeologic properties. Hydraulic conductivity and porosity of geologic units were adjusted until simulated particle arrival time at T4 and T5 were within an order of magnitude of first temporal moments from co-located ER pixels. Modeled streambed flux and RTD were calculated for the calibrated simulation (model run 6). Table 2 summarizes model runs, data used to parameterize subsurface architecture, and hydrogeologic parameterization.

Results

Development of Uncalibrated Subsurface Lithology Models

Geometry A: Soil and Geology Maps, Surface Observations

Soil and geologic maps and published studies from the upper hillslopes in the catchment indicate that the site

includes shale bedrock, overlain by weathered bedrock, and finally a layer of alluvial sediment (Shields and Sopper 1969). The subsurface architecture derived from this information is presented in Figure 3A, which includes a 1.4 m sediment layer and 3.2 m weathered shale layer, underlain by bedrock. The observed bedrock outcrop beginning at $X = 61$ m and continuing downstream was simulated as a vertical bedrock outcrop that terminated the longitudinal extent of both the soil and bedrock layers.

Geometry B: Depth to Refusal

At five locations in the study reach, a steel rod was driven into the bed to refusal (labeled i through v in Figure 2). Depth to refusal was interpreted as the depth to the interface between streambed sediment and weathered shale. The interface was linearly interpolated between observations and was assumed to terminate at the bedrock outcrop. Geometry B (Figure 3B) maintains the interface geometry between the bedrock and weathered shale; the interface between the sediment and weathered shale was modified to match field observations.

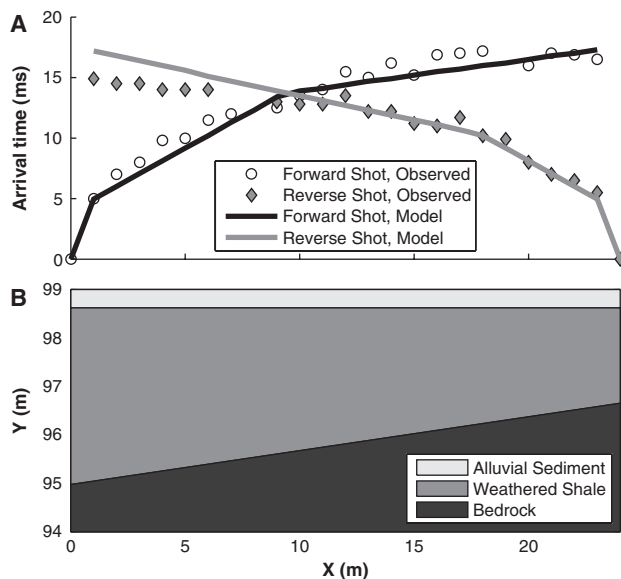


Figure 4. (A) Observed (points) and simulated (lines) arrival times for both forward (source at NW end of transect) and reverse (source at SE end of transect) shots along the seismic refraction transect. (B) Best-fit subsurface model, shown as a cross-section along the seismic transect, as modeled using REFRACT (Burger et al. 2006). The model includes a dipping bedrock layer, which agrees with observed bedrock outcropping at the downstream end of the study reach.

Geometry C: Seismic Refraction Survey

Data for the seismic transect were visually interpreted as a three-layer system (sediment, weathered shale, and bedrock), with an interface between the bottom two layers dipping from the southeast toward the northwest. The seismic model REFRACT was fit by manually adjusting dip angle and layer thicknesses to minimize the RMSE between observed and simulated seismic data for first arrival of seismic shots at each geophone. For the final seismic model (Figure 4B), average RMSE was calculated by REFRACT (Burger et al. 2006) as 0.96 ms. The dip angle for the best-fit model is 4° . For a surface velocity of 190.5 m/s, the surface topographic relief along the transect (0.57 m) could add up to 2.99 ms to a measurement. Both seismic model error and topographic deviation were considered negligible for the initial interpretation of the data. The seismic refraction model was used to modify the interface between bedrock and weathered shale layers (Figure 3C); all other geometry was preserved from Geometry B. The bedrock depths at T1 and T5, determined from the seismic study, were used to simulate a planar interface between bedrock and weathered shale layers. The bedrock interface was linearly interpolated downstream to the bedrock outcrop observed at the streambed.

Geometry D: Background ER Data

The average standard deviation between stacked measurements of ER was $0.085 \Omega\text{m}$ (0.08%) for the 35,856 measurements collected during the study. Average RMSE in the inverted images relative to the noise for T1,

T2, T3, T4, and T5 combined was 1.05%; RMSE ranged from 0.18% to 2.25%. Data for one transect (dashed line in Figure 1) did not invert to levels of RMSE that were comparable to the remaining transects, possibly owing to poor contact between electrodes and sediment generating noisy data, and was omitted from this study.

Pre-tracer subsurface models based on the ER data generally show a low resistivity layer underlain by a higher resistivity layer (Figure 5A through E), interpreted as weathered shale above bedrock based on ER images (Ward et al. 2010b). The weathered shale layer is approximately 3 m below the streambed at the upstream end of the study reach (Figure 5A, B), nearly gone in Figure 5C, and is not present in Figure 5D and E. The high resistivity location in the shallow subsurface ($X = 0$ to 6 m, Figure 5A) was interpreted as an abandoned streambed by Ward et al. (2010b), an explanation for which there is additional evidence in the continuity of that feature observed in subsequent transects (Figure 5B, C). Finally, the low resistivity layer interpreted as soil and weathered bedrock (Figure 5A, B) at depths of 0 to 3 m below the streambed appears to pinch-out in Figure 5C, and is replaced by a higher resistivity deposit in Figure 5D and E. ER data are interpreted as a less-weathered shale layer that was added to the subsurface model from Geometry C, resulting in a four-layer geometry (Figure 3D).

Geometry E: ER Monitoring of Solute Tracer

Subsurface models based on ER data collected during the peak of the tracer study (i.e., immediately before the solute injection was ended) show the presence of the saline tracer as a drop in resistivity compared to pre-tracer images (Figure 5F through J). Solute is generally present at the upstream and downstream ends of the study reach at depths of 0 to 1.5 m, with apparent upwelling upstream of T3 (Figure 5H) and downwelling downstream of that location. Starting with Geometry D, the lithological boundaries for the less-weathered bedrock layer were adjusted such that simulated particle tracking along flowpaths matched those observed with ER imaging of the solute at the locations of ER transects. Notably, the less-weathered bedrock layer was extended upstream to generate the shallower flowpaths observed at T1, and thickness was increased to create the up- and downwelling pattern observed at T3 through T5 (Figure 3E).

Flow Model Calibration Using Time-Lapse ER Monitoring

Time-lapse ER models during the tracer injection show that solute tracer first appears in the subsurface at T1 and T4 (Figure 6). A hyporheic zone of relatively constant width (about 1.5 m) grows throughout the injection period within the study reach, reaching a constant plateau, and slowly flushing of solute tracer. Visualization is based on interpolation between ER transects, and provides a qualitative assessment of hyporheic flowpath networks. Tracer predicted above the streambed is the result of flowpaths entering the subsurface from upstream of the study reach (i.e., flowpaths originating upgradient;

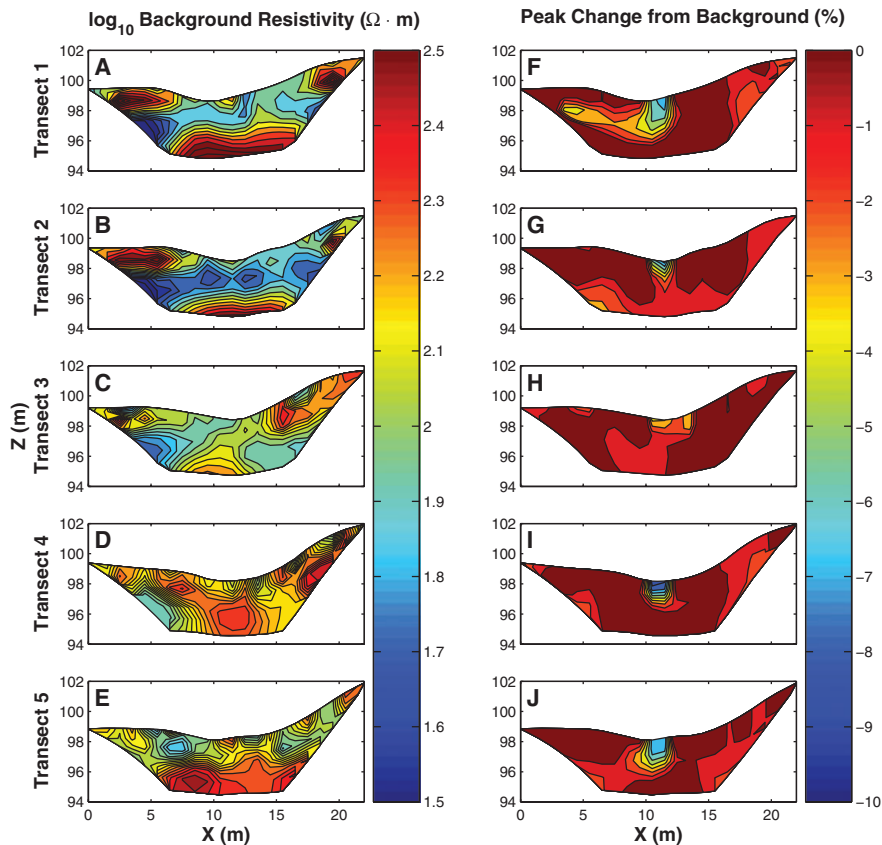


Figure 5. (A-E) Background (i.e., pre-tracer) ER imaging of subsurface structure. High resistivity regions are interpreted as bedrock. An apparent structural change exists between transects 2 and 5, interpreted as less-weathered shale. (F-J) Resistivity change from background (as percent) at the peak of the solute injection along each transect. Decreases in ER are interpreted as the presence of the tracer in the subsurface. The bedrock layer appears closer to the surface in transects 4 and 5 based on electrical properties (D-E). These changes in resistivity do not correspond with the location of the solute tracer (I-J), illustrating the difference between electrical properties of the subsurface and hydrogeologic properties of the subsurface. The geophysical observation of process dynamics is an important tool to inform numerical models of groundwater flow and transport, although changes in physical properties may not correspond to changes in hydrologic properties.

$X < 28$ m in Figure 6). The vertical space between the streambed and predicted solute plume in the subsurface ($X > 30$ m in Figure 6) may be a result of the spatial resolution of the geophysical inversions. Without direct sampling of the shallow subsurface, which we did not collect, we cannot know from the ER data if solute was present in this location. Interpolation over distances of 4 to 8 m is not purported to provide quantitative assessment between transects; heterogeneity between observations is likely to result in more complex flowpath networks.

Temporal moment analysis was completed for each pixel in the T4 and T5 inverted data sets. Mean arrival times (i.e., normalized first temporal moments) based on ER images of solute tracer range from 23 to 27 h in the shallow subsurface at T4 and T5 based on ER imaging (Figure 7). Simulated particle arrival times within 10 cm of this location in the X - and Z -directions are orders of magnitude larger for simulations using published hydrogeologic values (Figure 7). We calibrated the hydraulic conductivity and porosity for the soil and weathered shale layers using Geometry E (the most well-constrained subsurface model) until particle arrival times were within an order of magnitude of those observed using time-lapse

ER imaging in the shallowest 1.5 m of the subsurface. Calibration was achieved by manually adjusting hydraulic conductivity and porosity of the sediment and weathered shale layers, keeping the lithological boundaries fixed, to achieve the best agreement between normalized first temporal moments and simulated particle arrival time depth profiles at T4 and T5. Hydraulic conductivity of the sediment and weathered shale layers were increased incrementally by an order of magnitude (starting from assumed values in published literature) until particle arrival in the weathered shale layer was in the same order of magnitude as ER-derived mean arrival times. Using flowpath penetration as an initial metric, it was quickly recognized that the sediment and weathered-shale layers both needed to be higher in hydraulic conductivity. Our interpretation was that the depth to refusal measurements were not accurate, and the top two layers, taken together, represent the actual sediment layer in the field (i.e., the weathered shale layer and sediment layers should be taken as a single unit). Porosity for the layers was set to 25%, an increase from assumed values to account for the gravel observed at the streambed and in the shallow subsurface. Best fit was achieved for both the soil and weathered shale

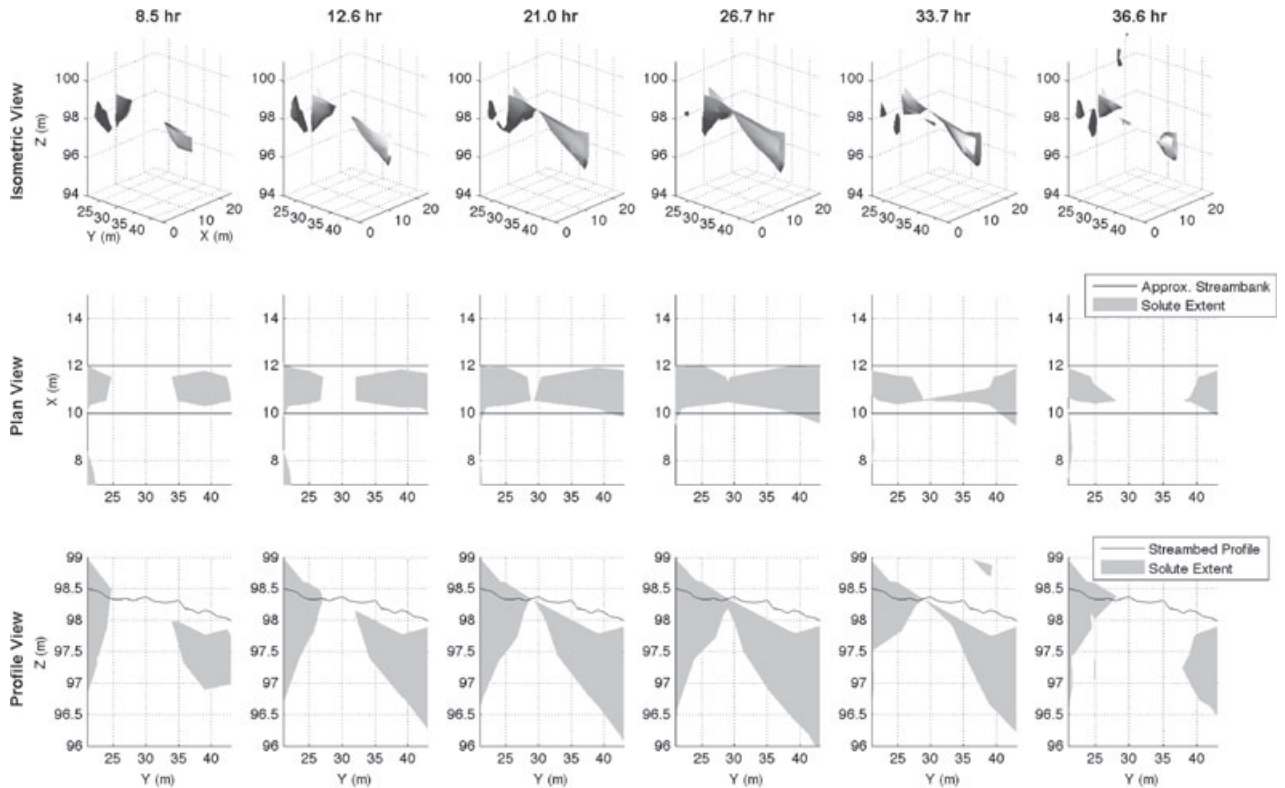


Figure 6. Time-lapse visualization of solute transport in the hyporheic zone, as linear interpolation between the two-dimensional (2D) inversions. In all figures, X is the cross-stream coordinate, Y the coordinate along the stream centerline, and Z is the vertical datum. Flow is from left to right in all images. Isometric (top row), plan (middle row), and profile (bottom row) views of the subsurface imaging are shown (on different scales). The approximate bank locations (middle row) and the stream profile (bottom row) are shown for reference. Solute enters the subsurface from the upstream end of the study reach and by downwelling near $Y = -9$ m. Imaging shows subsurface architecture causes upwelling near the center of the study reach. Hyporheic width is approximately constant and equal to the width of the stream through the study reach.

layers set at hydraulic conductivity and effective porosity of 8×10^{-5} m/s and 25%, respectively. These values are reasonable for the area; Kuntz et al. (2011) reports values as high as 10^{-5} m/s and 45% for the shallow subsurface in a nearby catchment. In summary, model runs 1 to 5 are each of the five geometries parameterized using uncalibrated hydrogeologic values; model run 6 is the calibrated Geometry E (model runs are summarized in Table 2).

Simulated Hyporheic Flux and Residence Times

The gross flux of water across the streambed for alternative subsurface models is summarized in Table 2. For model runs 1 to 5 (uncalibrated hydrogeologic parameters), streambed flux is largest for Geometry A, and decreases as the subsurface architecture is more completely characterized. This result is attributed to the decreasing thickness of the soil and weathered shale layers as subsurface architecture is constrained by the bedrock and less-weathered shale layers. In this setting, the increased thickness of the low-permeability layers both causes upwelling at the upstream end (similar to results suggested by Ward et al. 2011) and restricts downwelling flowpaths in the center of the stream. Model run 6 (the calibrated version of Geometry E) has streambed flux on the order of 10^{-4} m²/s (or m/s multiplied by a unit

streambed width), whereas model run 5 (the uncalibrated simulation of Geometry E) had streambed flux on the order of 10^{-7} m²/s.

Particle tracklines show the expected up- and downwelling pattern of hyporheic exchange that is expected from pool and riffle morphology (Figure 3). Added topography along the bedrock interface (Geometry C) and the location and extent of the less-weathered shale deposit (Geometry D, E) produce interactions between the individual flow-cells generated by surface topography. A complex network of both short and extensive hyporheic flowpaths is ultimately generated using Geometry E, which represents the best-constrained lithological boundaries (Figure 3E). Increasingly complex subsurface architecture resulted in longer particle residence times in the subsurface at T4 and T5 (Figure 7). Particles arrive at any given location in the subsurface more rapidly for the highly idealized Geometry A, while the inclusion of additional complexity resulted in later arrival at a given depth.

Model runs 1 to 5 produce similar RTDs despite substantial changes in subsurface architecture (Figure 8); the unchanged hydraulic parameterization of the subsurface results in very similar RTDs. The inclusion of solute transport data for model calibration, however, resulted in

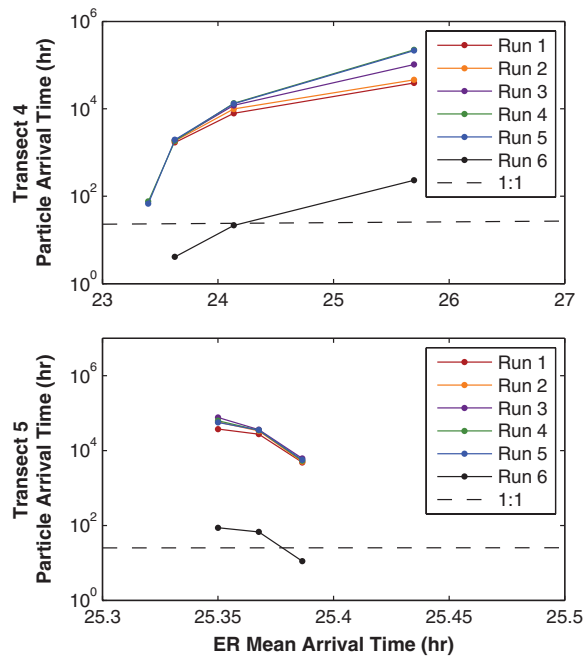


Figure 7. Particle arrival times within 10 cm of ER transects 4 (top) and 5 (bottom) vs. ER-derived mean arrival times for both uncalibrated (runs 1 to 5) and calibrated hydrogeologic parameters (run 6). Each point represents a single ER pixel at the stream centerline. Values for a perfectly calibrated model should plot on a 1:1 line (i.e., a perfect fit between model and observed data). Calibrated models produce results that match mean arrival times determined from time-lapse ER imaging within an order of magnitude; further refinement of heterogeneity within each layer (as opposed to only adjusting homogeneous, isotropic parameters for the geologic units included) could further improve model performance.

a shifted RTD because of the change in hydraulic conductivity and porosity. Model runs 1 to 5 have median residence times on the order of 10^3 h, whereas model run 6 has a median residence time on the order of 10^0 h (Figure 8; Table 2). While median residence times are fairly uniform for model runs 1 to 5, mean residence times vary from 9.5×10^4 to 1.3×10^{10} h. Increasingly well-resolved subsurface structure led to an increase in the longest timescale flowpaths, resulting in later mean arrival times. The transport of a small number of particles through the unweathered bedrock model domain accounts for this shift in mean values. Increasing subsurface complexity increases the variance in particle residence times (Table 2), with Geometries A and E producing RTD variance on the order 10^{10} and 10^{15} h² for uncalibrated hydrogeologic parameters. The calibrated model produced RTD variance on the order 10^{21} h².

Discussion

Comparison of Subsurface Architecture Characterization Methods

The suite of subsurface characterization techniques applied in this study provides differing interpretations of

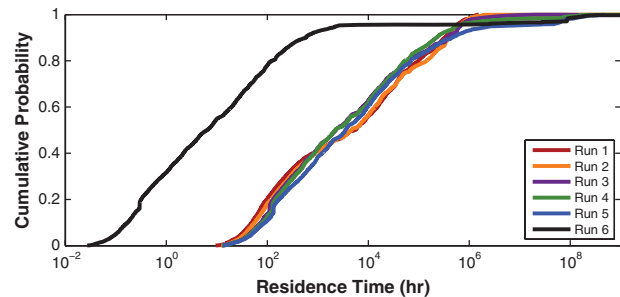


Figure 8. Cumulative distributions of particle residence times for model runs using uncalibrated (runs 1 to 5) and calibrated (run 6) values of hydraulic conductivity and porosity. Uncalibrated models produced RTDs shifted approximately three orders of magnitude later than those using calibrated values. Increasingly complex subsurface architecture results in a wider distribution of subsurface residence times, ultimately generating some significantly longer flowpaths in the most well-constrained geometries.

subsurface architecture, which do not all agree. Seismic refraction, background ER, and field observations of bedrock outcropping suggest a confining layer that is generally deeper at the upstream end of the study reach and that outcrops at the downstream end of the study reach. Depth to refusal, background ER, and ER imaging of solute tracer all suggest that some geologic structure exists in the shallow subsurface near T3; only ER imaging of solute tracer and depth to refusal characterize features that suggest downwelling downstream of this location. Based on ER data, this structure causes upwelling of the deepest flowpaths from upstream. Particle tracking suggests that downwelling of shorter flowpaths also occurs near this area.

The shallow subsurface characterization using depth to refusal measurements provided a limited characterization of subsurface architecture, based on agreement with other investigation methods. These observations may have been complicated by the presence of large cobbles and boulders in the subsurface. In the best-fit simulations, the streambed sediment and weathered bedrock layers were parameterized identically, suggesting the interface inferred from depth to refusal was erroneous. The two, combined, might accurately represent the actual sediment layer in the field, with the “less-weathered bedrock” layer in the Geometry E representing the actual extent of the weathered shale. Finally, a more detailed study at the site could consider topography along the interface between weathered shale and bedrock layers, which could cause large-scale patterns of up- and downwelling (Ward et al. 2011).

Electrical imaging of process dynamics (i.e., solute transport) provides more information on lithology and subsurface heterogeneity than characterizing process areas (i.e., static features) alone. Time-lapse images of solute tracer enhanced the interpretation of subsurface architecture by highlighting both temporal trends in tracer arrival and by illustrating downwelling in a location that was

not identified in background ER alone (i.e., downstream of T3). Although background electrical properties in the subsurface appear to change from upstream (T1, T2) to downstream (T3, T4, T5), we conclude these changes are related to electrical properties of the soil-water matrix (i.e., ER) rather than hydrogeologic parameters such as permeability or hydraulic conductivity. This conclusion is based on similar observed solute transport both at upstream (T1-T2) and downstream (T4-T5) ER transects, which had different ER values during background (i.e., pre-tracer) conditions. Background ER measurements are a function of electrical properties of the soil-water matrix in the subsurface, but they do not accurately represent the variables that control flow and transport through porous media (i.e., hydraulic conductivity, porosity). The conflicting interpretations of electrical properties and observed transport illustrate the difficulty in assigning hydrogeologic properties based on geophysical studies of process areas alone, a problem which is unique neither to this site nor method (see reviews by Lesmes and Friedman 2005; Pride 2005). The ability of ER to directly monitor the transport of solutes in the subsurface identifies transport phenomena that would have been overlooked using static ER images alone.

The Utility of Geophysical Investigation to Characterize Subsurface Architecture

The application of geophysical methods to characterize subsurface architecture reduces, to some extent, the uncertainty in numerical models of groundwater flow by informing process areas and dynamics in the subsurface. With this improvement comes the inherent assumption that geophysical data are accurate; it must be acknowledged here that geophysical data, particularly those that result from inversion processes, are subject to uncertainty that is carried forward into hydrologic models. Despite this uncertainty, we suggest the inclusion of geophysical investigations to inform models of subsurface flow and transport is an improvement to numerical models of subsurface flow and transport in two ways. First, geophysical investigation of subsurface architecture (i.e., process areas) is spatially distributed, characterizing lithological boundaries. Although geophysical methods rely on simplifying assumptions and/or data inversion to characterize the subsurface, they are able to inform major geologic boundaries and layer thicknesses distributed throughout the domain. Second, time-lapse monitoring of transport (i.e., process dynamics) provides a data set that characterizes solute transport with high spatial (relative to monitoring well networks) and temporal resolution. The use of coupled geophysical monitoring and solute tracer studies shows promise for monitoring of transport along flowpaths and allowed calibration of a model that matched the distributed transport properties observed in the field. We underscore here that, while both benefits improve the realism of numerical models (in comparison to common assumptions of a homogeneous, isotropic subsurface), the interpretation of geophysical data is still limited by inherent uncertainty in the techniques.

Despite the promise of geophysically monitoring subsurface architecture and transport dynamics, the use of these methods is not sufficient to completely characterize all subsurface transport and hydrogeologic properties at all scales. In our study, the calibrated model was only able to corroborate particle tracking and ER data within an order of magnitude. Although this is a clear advance over models based on published or estimated hydrogeologic values, it is not sufficient to make predictions at the scale of individual flowpaths (i.e., individual particles). Heterogeneity within the simulated geologic units and/or increased resolution of measurements would be necessary to achieve a better match between ER and model results. Finally, we note that ER data have large and poorly resolved support volumes; comparison of these data with particle tracking may never yield perfect results because of the disparity of measurement support volumes. The application of geophysical methods demonstrated in this study focuses on the characterization of subsurface architecture (i.e., the changes in geologic properties occurring at scales on the order of 10^{-1} m and larger). The exact resolution and uniqueness of results for geophysical studies like those presented in this study are subject to a variety of assumptions made in the collection and interpretation processes (see review by Linde et al. 2006). Still, these methods provide information about subsurface structure and transport that cannot be readily obtained using traditional solute tracers and sparse monitoring well networks, and which has a direct effect on predicted RTDs and streambed flux.

The application of ER imaging of solute tracer to models of hyporheic exchange allows increasingly well-resolved parameterization of subsurface architecture (i.e., lithological boundaries). By calibrating models to observed process dynamics, increasingly realistic simulations of RTDs and flowpath network extent are expected. This improved simulation is an advance toward the goal of more accurately quantifying of hyporheic flow and transport at the scale of individual flowpaths. While our objective was to characterize the role of macroscale heterogeneities (i.e., those on the order of 10^{-1} m and larger), Pollock and Cirpka (2010) demonstrated the coupled inversion of flow and ER data collected during a solute tracer study might also be used to characterize smaller scale hydraulic conductivity distributions in the subsurface.

Conclusions

The objective of this study was to determine how increasingly better resolved lithological boundaries in the subsurface affect predictions of streambed flux and hyporheic RTDs. Our work demonstrates that increasingly complex subsurface architectures generate more variable RTDs (i.e., wider distributions). Simulated streambed flux was also lower for more complex subsurface architectures in our study; this result demonstrates the variability in model predictions as a function of subsurface characterization. We expect other geometries exist where increasing

resolution of subsurface lithology could yield opposing results. Results suggest that highly idealized subsurface characterizations (e.g., homogeneous and isotropic geologic units with single geologic units, or without topography along lithological boundaries) could over- or underestimate hyporheic exchange flux and RTDs as a function of subsurface structure and complexity in permeability distributions (e.g., Sawyer and Cardenas 2009).

We demonstrated the integration of coupled solute injection and ER imaging studies along with other common shallow subsurface investigation techniques to construct and calibrate numerical models of hyporheic exchange. The combined use of multiple geophysical methods allowed better spatial resolution of lithological boundaries in the subsurface, and allowed calibration of the model to match transport observed with time-lapse ER monitoring of saline tracer. ER monitoring of solute tracer studies was used to infer both subsurface architecture and transport properties that were not otherwise be observable, leading to better calibrated flow and transport models that include macroscale heterogeneity in the subsurface. Without ER calibration, models predicted orders of magnitude less streambed flux and longer residence time along hyporheic flowpaths. Pseudo-3D time-lapse visualization of hyporheic flowpaths provides a conceptual model from which additional characterization of subsurface architecture can be inferred. Finally, we have demonstrated the promise of geophysical monitoring of transport dynamics as a first step toward reducing equifinality in groundwater flow models.

Acknowledgments

This material is based upon work supported by the National Science Foundation under grant nos. EAR-0911435 and EAR-0747629. Any opinions, findings, and conclusions or recommendations expressed in this material are those of the authors and do not necessarily reflect the views of the National Science Foundation. Our thanks to Dr. Elizabeth Boyer and the U.S. Forest Service for support of this work at the Leading Ridge Watershed Research Unit site. The Penn State University Spring 2010 Environmental Geophysics class and instructor Dr. Andy Nyblade contributed to the seismic refraction study. Julianne Hagarty and Nathan Barber assisted with collection and inversion of geophysical data. Our thanks to Dr. Audrey Sawyer and two anonymous reviewers whose insight improved the quality of this manuscript.

References

Advanced Geosciences, Inc. 2008. Instruction Manual for EarthImager 2D v2.3.0.

Anderson, J., S. Wondzell, M. Gooseff, and R. Haggerty. 2005. Patterns in stream longitudinal profiles and implications for hyporheic exchange flow at the H. J. Andrews Experimental Forest, Oregon, USA. *Hydrological Processes* 19, no. 15: 2931–2949.

Bevc, D., and H. Morrison. 1991. Borehole-to-surface electrical resistivity monitoring of a salt water injection experiment. *Geophysics* 56, no. 6: 769–777.

Beven, K. 2006. A manifesto for the equifinality thesis. *Journal of Hydrology* 320, no. 1–2: 18–36.

Binley, A., G. Cassiani, and R. Deiana. 2010. Hydrogeophysics: Opportunities and challenges. *Bollettino di Geofisica Teorica ed Applicata* 51, no. 4: 267–284.

Binley, A., S. Henry-Poulter, and B. Shaw. 1996a. Examination of solute transport in an undisturbed soil column using electrical resistance tomography. *Water Resources Research* 32, no. 4: 763–769.

Binley, A., B. Shaw, and S. Henry-Poulter. 1996b. Flow pathways in porous media: Electrical resistance tomography and dye staining image verification. *Measurement Science and Technology* 7: 384.

Boulton, A., T. Datry, T. Kasahara, M. Mutz, and J. Stanford. 2010. Ecology and management of the hyporheic zone: Stream–groundwater interactions of running waters and their floodplains. *Journal of the North American Benthological Society* 29, no. 1: 26–40.

Bredehoeft, J., and L. Konikow. 1993. Ground water models: Validate or invalidate. *Ground Water* 31, no. 2: 178–179.

Brosten, T.R., J.H. Bradford, J.P. McNamara, M.N. Gooseff, J.P. Zarnetske, W.B. Bowden, and M.E. Johnston. 2009. Estimating 3D variation in active-layer thickness beneath arctic streams using ground-penetrating radar. *Journal of Hydrology* 373, no. 3–4: 479–486.

Brunke, M., and T. Gonser. 1997. The ecological significance of exchange processes between rivers and groundwater. *Freshwater Biology* 37: 1–33.

Brunner, G. 2006. HEC-RAS River Analysis System User's Manual (Version 4.0 Beta). *US Army Corps of Engineers Hydrologic Engineering Center (HEC)*.

Burger, H.R., A.F. Sheehan, and C.H. Jones. 2006. *Introduction to Applied Geophysics: Exploring the Shallow Subsurface*. New York: WW Norton.

Cardenas, M., J. Wilson, and V. Zlotnik. 2004. Impact of heterogeneity, bed forms, and stream curvature on subchannel hyporheic exchange. *Water Resources Research* 40, no. 8: W08307.

COMSOL, Inc. 2008. version 3.5, *User's Guide and Reference Guide*. Burlington, Massachusetts: COMSOL.

Crook, N., A. Binley, R. Knight, D. Robinson, J. Zarnetske, and R. Haggerty. 2008. Electrical resistivity imaging of the architecture of sub-stream sediments. *Water Resources Research* 44.

Day-Lewis, F., K. Singha, and A. Binley. 2005. Applying petrophysical models to radar travel time and electrical resistivity tomograms: Resolution-dependent limitations. *Journal of Geophysical Research* 110, no. B8: B08206.

Friedel, S. 2003. Resolution, stability and efficiency of resistivity tomography estimated from a generalized inverse approach. *Geophysical Journal International* 153, no. 2: 305–316.

Gooseff, M.N., J.K. Anderson, S.M. Wondzell, J. LaNier, and R. Haggerty. 2006. A modelling study of hyporheic exchange pattern and the sequence, size, and spacing of stream bedforms in mountain stream networks, Oregon, USA. *Hydrological Processes* 20, no. 11: 2443–2457.

Hassan, A.E. 2004. Validation of numerical ground water models used to guide decision making. *Ground Water* 42, no. 2: 277–290.

Hester, E.T., and M.W. Doyle. 2008. In-stream geomorphic structures as drivers of hyporheic exchange. *Water Resources Research* 44.

Jones, K.L., G.C. Poole, W.W. Woessner, M.V. Vitale, B.R. Boer, S.J. O'Daniel, S.A. Thomas, and B.A. Geffen. 2008. Geomorphology, hydrology, and aquatic vegetation drive seasonal hyporheic flow patterns across a gravel dominated floodplain. *Hydrological Processes* 22, no. 13: 2105–2113.

Kasahara, T., and S.M. Wondzell. 2003. Geomorphic controls on hyporheic exchange flow in mountain streams. *Water Resources Research* 39, no. 1: 1005.

- Kemna, A., B. Kulesa, and H. Vereecken. 2002. Imaging and characterisation of subsurface solute transport using electrical resistivity tomography (ERT) and equivalent transport models. *Journal of Hydrology* 267, no. 4: 125–146.
- Koch, K., J. Wenninger, S. Uhlenbrook, and M. Bonell. 2009. Joint interpretation of hydrological and geophysical data: Electrical resistivity tomography results from a process hydrological research site in the Black Forest Mountains, Germany. *Hydrological Processes* 23, no. 10: 1501–1513.
- Konikow, L.F., and J.D. Bredehoeft. 1992. Ground-water models cannot be validated. *Advances in Water Resources* 15, no. 1: 75–83.
- Kostelnik, K., J. Lynch, J. Grimm, and E. Corbett. 1989. Sample size requirements for estimation of throughfall chemistry beneath a mixed hardwood forest. *Journal of Environmental Quality* 18, no. 3: 274–280.
- Krause, S., D. Hannah, J. Fleckenstein, C. Heppell, D. Kaeser, R. Pickup, G. Pinay, A. Robertson, and P. Wood. 2010. Interdisciplinary perspectives on processes in the hyporheic zone. *Ecohydrology* 4, no. 4: 481–499.
- Kuntz, B., S. Rubin, B. Berkowitz, and K. Singha. 2011. Quantifying solute transport behavior at the Shale Hills Critical Zone Observatory. *Vadose Zone Journal* 10, 15 p. DOI:10.2136/vzj2010.0130.
- Lautz, L., and D. Siegel. 2006. Modeling surface and ground water mixing in the hyporheic zone using MODFLOW and MT3D. *Advances in Water Resources* 29, no. 11: 1618–1633.
- Lesmes, D.P., and S.P. Friedman. 2005. Relationships between the electrical and hydrogeological properties of rocks and soils. In *Hydrogeophysics*, ed. Y. Rubin and S.S. Hubbard, 87–128. Dordrecht, the Netherlands: Springer.
- Linde, N., J. Chen, M.B. Kowalsky, and S. Hubbard. 2006. Hydrogeophysical parameter estimation approaches for field scale characterization. In *Applied Hydrogeophysics*, ed. H. Vereecken, A. Binley, G. Cassiani, A. Revil, and K. Titov, 9–44. Dordrecht, the Netherlands: Springer.
- Lynch, J., and E. Corbett. 1989. Hydrologic control of sulfate mobility in a forested watershed. *Water Resources Research* 25, no. 7: 1695–1703.
- Lynch, J.A., C.M. Hanna, and E.S. Corbett. 1986. Predicting pH, alkalinity, and total acidity in stream water during episodic events. *Water Resources Research* 22, no. 6: 905–912.
- Mayes, M., P. Jardine, I. Larsen, S. Brooks, and S. Fendorf. 2000. Multispecies transport of metal-EDTA complexes and chromate through undisturbed columns of weathered fractured saprolite. *Journal of Contaminant Hydrology* 45, no. 3–4: 243–265.
- Naegeli, M.W., P. Huggenberger, and U. Uehlinger. 1996. Ground penetrating radar for assessing sediment structures in the hyporheic zone of a Prealpine river. *Journal of the North American Benthological Society* 15, no. 3: 353–366.
- Nyquist, J., P. Freyer, and L. Toran. 2008. Stream Bottom Resistivity Tomography to Map Ground Water Discharge. *Ground Water* 46, no. 4: 561–569.
- Oreskes, N., K. Shrader-Frechette, and K. Belitz. 1994. Verification, validation, and confirmation of numerical models in the earth sciences. *Science* 263: 4.
- Packman, A.I., and M. Salehin. 2003. Relative roles of stream flow and sedimentary conditions in controlling hyporheic exchange. *Hydrobiologia* 494, no. 1: 291–297.
- Pollock, D., and O. Cirpka. 2010. Fully coupled hydrogeophysical inversion of synthetic salt tracer experiments. *Water Resources Research* 46, no. 7: W07501.
- Pride, S.R. 2005. Relationships between seismic and hydrological properties. In *Hydrogeophysics*, ed. Y. Rubin and S.S. Hubbard, 253–290. Dordrecht, the Netherlands: Springer.
- Rishel, G.B., J.A. Lynch, and E. Corbett. 1982. Seasonal stream temperature changes following forest harvesting. *Journal of Environmental Quality;(United States)* 11, no. 1: 112–116.
- Ryan, R.J., and M.C. Boufadel. 2006. Influence of streambed hydraulic conductivity on solute exchange with the hyporheic zone. *Environmental Geology* 51, no. 2: 203–210.
- Saenger, N., P.K. Kitanidis, and R.L. Street. 2005. A numerical study of surface–subsurface exchange processes at a riffle-pool pair in the Lahn River, Germany. *Water Resources Research* 41.
- Salehin, M., A.I. Packman, and M. Paradis. 2004. Hyporheic exchange with heterogeneous streambeds: Laboratory experiments and modeling. *Water Resources Research* 40, no. 11: W11504.
- Sawyer, A., and M. Cardenas. 2009. Hyporheic flow and residence time distributions in heterogeneous cross-bedded sediment. *Water Resources Research* 45, no. 8: W08406.
- Schima, S., D.J. LaBrecque, and P.D. Lundegard. 1996. Monitoring air sparging using resistivity tomography. *Ground Water Monitoring & Remediation* 16, no. 2: 131–138.
- Sevan, W.D., 2000, Map 13: Physiographic Provinces of Pennsylvania. Bureau of Topographic and Geologic Survey, Department of Conservation and Natural Resources, Commonwealth of Pennsylvania.
- Shields, R.R., and W.E. Sopper. 1969. An application of surface geophysical techniques to the study of watershed hydrology. *JAWRA Journal of the American Water Resources Association* 5, no. 3: 37–49.
- Singha, K., and S. Moysey. 2006. Accounting for spatially variable resolution in electrical resistivity tomography through field-scale rock-physics relations. *Geophysics* 71, no. 4: A25.
- Singha, K., A. Pidlisecky, F. Day-Lewis, and M. Gooseff. 2008. Electrical characterization of non-Fickian transport in groundwater and hyporheic systems. *Water Resources Research* 44, no. 3.
- Slater, L., A. Binley, and D. Brown. 1997. Electrical imaging of fractures using ground-water salinity change. *Ground Water* 35, no. 3: 436–442.
- Slater, L., A. Binley, W. Daily, and R. Johnson. 2000. Cross-hole electrical imaging of a controlled saline tracer injection. *Journal of Applied Geophysics* 44, no. 2–3: 85–102.
- Slater, L., A. Binley, R. Versteeg, G. Cassiani, R. Birken, and S. Sandberg. 2002. A 3D ERT study of solute transport in a large experimental tank. *Journal of Applied Geophysics* 49, no. 4: 211–229.
- U.S. Department of Agriculture, Natural Resources Conservation Service. 2008. Soil Survey of Huntingdon County, Pennsylvania. Version 3. <http://websoilsurvey.nrcs.usda.gov> (accessed March 28, 2010).
- Vaux, W.G. 1968. Intragravel flow and interchange of water in a streambed. *Fishery Bulletin* 66, no. 3: 479.
- Ward, A., M.N. Gooseff, and K. Singha. 2010a. Characterizing hyporheic transport processes-Interpretation of electrical geophysical data in coupled stream-hyporheic zone systems during solute tracer studies. *Advances in Water Resources* 33, no. 11: 1320–1330. DOI:10.1016/j.advwatres.2010.05.008.
- Ward, A.S., M.N. Gooseff, and K. Singha. 2010b. Imaging hyporheic zone solute transport using electrical resistivity. *Hydrological Processes* 24, no. 7: 948–953.
- Ward, A.S., M.N. Gooseff, and P.A. Johnson. 2011. How can subsurface modifications to hydraulic conductivity be designed as stream restoration structures? Analysis of

- Vaux's conceptual models to enhance hyporheic exchange. *Water Resources Research*. DOI: 10.1029/2010WR010028.
- White, P.A. 1988. Measurement of ground water parameters using salt water injection and surface resistivity. *Ground Water* 26, no. 2: 179–186.
- Wondzell, S., J. LaNier, R. Haggerty, R. Woodsmith, and R. Edwards. 2009. Changes in hyporheic exchange flow following experimental wood removal in a small, low-gradient stream. *Water Resources Research* 45 no. 5: W05406.
- Wroblicky, G.J., M.E. Campana, H.M. Valett, and C.N. Dahm. 1998. Seasonal variation in surface-subsurface water exchange and lateral hyporheic area of two stream-aquifer systems. *Water Resources Research* 34, no. 3: 317–328.